Applied Ocean Research 148 (2024) 104016

Contents lists available at ScienceDirect

Applied Ocean Research

journal homepage: www.elsevier.com/locate/apor

Numerical modelling of ship-generated solitary waves

Momchil Terziev *, Atilla Incecik

Department of Naval Architecture, Ocean and Marine Engineering, Henry Dyer Building, University of Strathclyde, 100 Montrose Street, Glasgow, UK

ARTICLE INFO

Keywords:
Ship resistance
URANS
Solitary waves
Shallow water
Confined water

ABSTRACT

A ship sailing at the wave speed in shallow water produces a complex wave pattern including a downstream disturbance in addition to a periodically generated upstream disturbance. The upstream component consists of solitary waves which are generated at the ship bow and emitted forward as soon as the local water depth is sufficiently modified enabling them to bypass the shallow water wave speed limit. Reynolds Averaged Navier-Stokes numerical simulations are carried out to explore this phenomenon in a fully non-linear and viscous virtual towing tank in cases where a ship sails at the waterway centreline as well as off-centreline conditions. Results indicate that friction attains no more than approximately 25 % of the total resistance coefficient, justifying the use of inviscid methods by previous studies in the literature. Water depth may have a significant impact on the frequency and amplitude of ship-generated solitary waves, but the manner in which this occurs is highly sensitive to the width of the waterway.

1. Introduction

When a vessel advances at a constant speed, a well-known V-shaped pattern of waves is emitted aft known as the Kelvin wake which makes an angle of approximately 19.47° relative to the vessel's centreline. Unlike deep waters, the shallow water wave pattern can broaden and theoretically become perpendicular to the vessel centreline (Havelock, 1908) when the depth Froude number is equal to unity ($F_h = V/\sqrt{gh}$ with V being the vessel speed, $\sqrt{gh}$ the wave speed, $g = 9.81$ m/s^2 and h is the water depth). That prediction according to linear theory is somewhat accurate with experiments showing that the aforementioned angle increases rapidly at $F_h = 1$ and decreases again thereafter. However, a second and more interesting phenomenon manifests in such cases, the emission of waves upstream even though the vessel advances at the wave speed.

The upstream emitted waves are known as solitary waves and have a peculiar set of properties that make them distinct from wind and ship generated waves found within the Kelvin wake. Much research has investigated the phenomenon of solitary wave radiation as shown in section 2. The same section also shows that there is a poorly understood relationship between the blockage (ratio of vessel's maximum cross section and waterway cross-section) and the energy contained within radiated waves. The authors' discovery that such waves are observed on Scottish canals today, where solitary waves were first discovered in the 1800s motivated the present study into the effects of blockage on solitary waves. In addition, to the best of the authors' knowledge, no previous work has investigated solitary wave radiation by a vessel using an Unsteady Reynolds Averaged Navier-Stokes (URANS) approach.

The remainder of the present paper is organised as follows. Section 2 contains a brief historical timeline around the discovery of solitary waves and subsequent research development. Sections 3 and 4 are dedicated to an outline of the selected case studies and numerical methods used, respectively. These are followed by results and discussion in Section 5. Finally, conclusions and identified gaps for future research are given in Section 6.

2. Background

Solitary waves were discovered by John Scott Russel in 1834 on Scotland's manually-dug canals, originally named 'wave of translation' (Russell, 1845). The primary motivation for the present study is the authors' discovery that solitary waves are still observed on Scotland's canals. Solitary waves are sometimes refereed to 'solitons' – a term coined by Zabusky and Kruskal (1965) to describe solutions of the Korteweg-de Vries equation which predict a special class of unidirectional waves may pass through each other without any permanent loss of 'identity', suffering only phase shifts. It is Zabusky and Kruskal's (1965) work that sparked research in solitary waves (Miles, 1980). As shown subsequently, experimental research documenting ship solitary waves

* Corresponding author.
E-mail address: momchil.terziev@strath.ac.uk (M. Terziev).

https://doi.org/10.1016/j.apor.2024.104016
Received 31 July 2023; Received in revised form 12 April 2024; Accepted 15 April 2024

Table 1
Principal dimensions of the Wigley hull.

Parameter	Symbol	Value	Units
Length	L	3	m
Beam	B	0.3	m
Draft	T	0.1875	m
Midship sectional area coefficient	C_M	0.64	–
Displacement	∇	0.076	m^3

initiated a flurry of activity in the 1980s.

Among the earliest experimental campaigns documenting upstream advancing disturbances produced by a ship was conducted by Thews and Landweber (1935). To the best of the authors' knowledge, little research was conducted on this phenomenon for several decades, until experimental work at Berkeley re-discovered ship-generated solitary waves in 1978 (Ertekin et al., 1986). For example, Huang et al. (1982) provided experimental data for the period of upstream emitted waves. Unlike the majority of research conducted since, the aforementioned authors investigated a large range of speeds, spanning form $F_h = 0.1$ to approximately $F_h = 1.1$. Their findings include the fact that ships can radiate upstream waves even at very low speeds, as low as $F_h = 0.1$, but the amplitude of these waves is small. More importantly, Huang et al. (1982) were able to rule out the effects viscosity and poor carriage speed control as the cause of ship-generated upstream waves, which were key suspects for the production of solitary waves up to that time.

Wu and Wu (1982) used the forced Boussinesq long-wave approximation to model the propagation of a pressure field at the critical depth Froude number. Their results showed that periodic upstream radiation

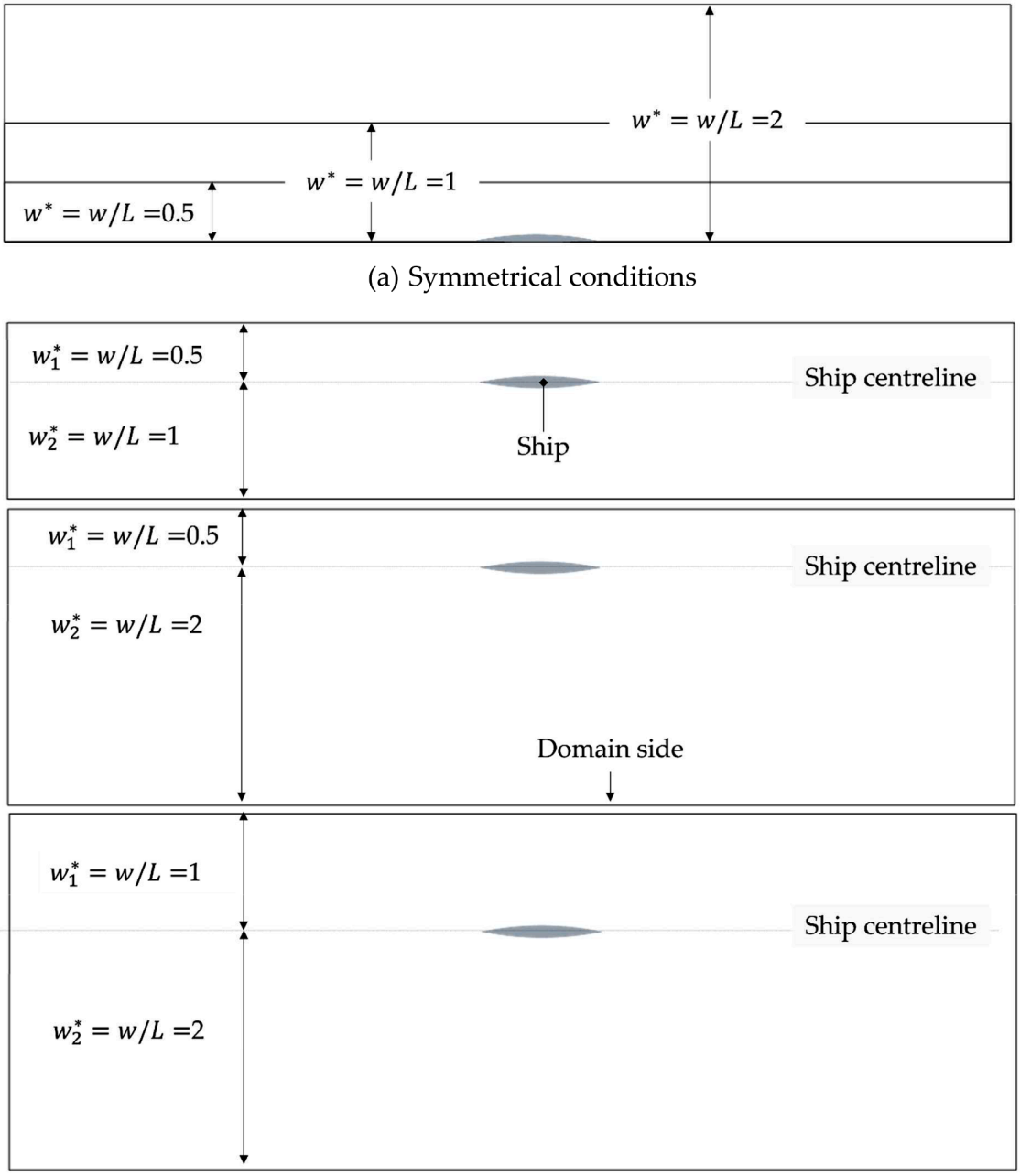

Fig. 1. Schematic diagram of the investigated conditions.

Table 2
Test matrix used in the present study. w_1 and w_2 are the port and starboard distance, respectively, and $w^*_{1,2}$ is the distance made dimensionless with the ship length ($w^* = w/L$). The blockage is defined as the ratio of the ship's maximum cross sectional area ($C_M BT$) and the waterway cross sectional area.

Case Number	$w^*_1 = w_1/L$	$w^*_2 = w_2/L$	Blockage	h/T	F_h
1	2	2	0.0582	1.1	1
2	2	1	0.0194		
3	2	0.5	0.0233		
4	1	1	0.0291		
5	1	0.5	0.0388		
6	0.5	0.5	0.0582		
7	2	2	0.0133	1.2	
8	2	1	0.0178		
9	2	0.5	0.0213		
10	1	1	0.0267		
11	1	0.5	0.0356		
12	0.5	0.5	0.0533		
13	2	2	0.0123	1.3	
14	2	1	0.0164		
15	2	0.5	0.0197		
16	1	1	0.0246		
17	1	0.5	0.0328		
18	0.5	0.5	0.0492		

of waves occurs. Later, Akylas (1984) used a forced Korteweg-de Vries equation to show that a pressure distribution can generate upstream advancing solitary waves at the critical speed ($F_h = 1$). He found good agreement with the experimental results of Huang et al. (1982) despite using a two dimensional approach. Unlike some earlier studies using linear theory, where waves continually grow as they travel upstream, the results of Akylas (1984) remained bounded with time.

To the best of the authors' knowledge, Ertekin et al. (1984a) were the first to suggest a link between the blockage coefficient and the radiation of solitary waves. Later, Cole (1985) showed that solitary waves may be produced at $F_h = 1$ by a submerged bump within a two-dimensional framework. His results, in conjunction with the calculations of Huang et al. (1982) seemed to rule out three-dimensionality as the cause of upstream radiation of waves. These two-dimensional frameworks can only reproduce the phenomenon at $F_h \approx 1$. As discussed by Akylas (1984), when the body or pressure field speed is equal to $\sqrt{gh}$, "…*the energy transferred by the travelling pressure distribution to the water cannot be radiated away from the source owing to the fact that the group velocity of the generated waves approaches*…" the speed of the object.

Mei (1986) developed a one-dimensional theory to investigate the effects of width on ship solitary wave radiation, finding that near $F_h = 1$, solitary waves are radiated even if the channel width is greater than the ship length. Around the same time, Ertekin et al. (1986) presented three dimensional calculations of ship-generated solitary wave using Green-Naghdi equations. Since it is unclear how a blockage factor can be calculated for a pressure field acting on a free surface, Miles (1986) suggested an equivalent bump with cross-sectional area $A = P/\rho g$, with P being the pressure distribution and ρ the water density. Using this parameter in 2D to represent the equivalent cross-sectional area and the depth Froude number, Miles (1986) suggested a trans-critical range within which no steady flow exists. Later, Mei and Choi (1987) extended Mei's (1986) theory to calculate the forces acting on a slender body near $F_h = 1$. Similarly, Pedersen (1988) used a simplified version of the Kadomtsev-Petviashvili (KP) equation to investigate trans-critical wave resistance.

As discussed above, a link is thought to exist between the blockage and the conditions necessary to generate solitary waves. In addition, the critical speed, $F_h = 1$ can be achieved for a range of depths and speeds meaning that the conditions sufficient for solitary wave production can be created for a range of conditions. Lataire et al. (2012) used conservation of mass and energy to show that a range of such trans-critical depth Froude numbers exist for a given blockage. This trans-critical region lies above a critical curve (shown in Eq. (1)) and is characterised by the inability of the flow to satisfy steady state conservation of mass and energy.

$$m = 1 - \sin\left(3\arcsin\left(\frac{F_h^{2/3}}{2}\right)\right) \tag{1}$$

Eq. (1) predicts that steady flow at $F_h = 1$ is impossible for any blockage. That condition is therefore convenient to use while varying

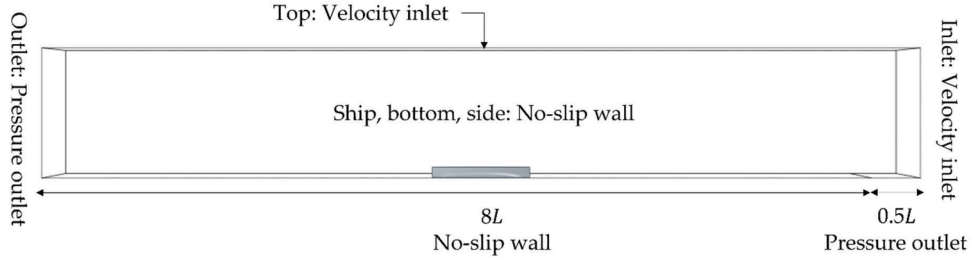

Fig. 2. Computational domain and boundary conditions.

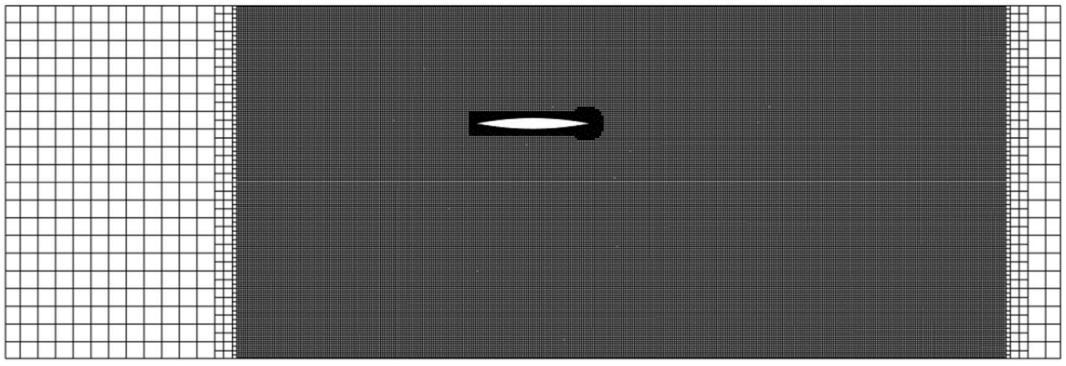

Fig. 3. Computational mesh on the mean water surface used for case 2 ($h/T = 1.1$, $w^*_1 = 2$, $w^*_2 = 1$).

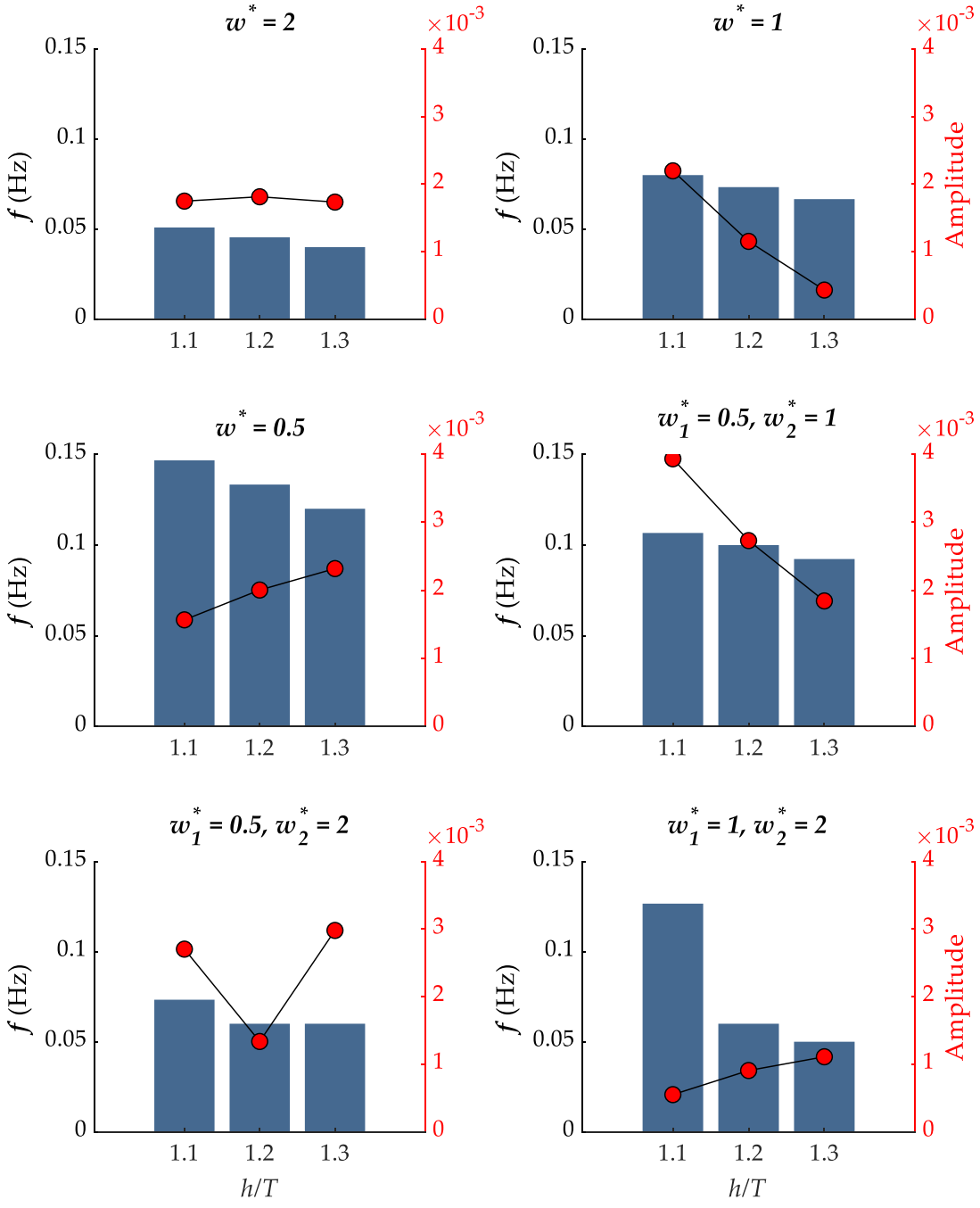

Fig. 4. Frequency and amplitude of oscillation of the total resistance coefficient for all cases, obtained using FFT analysis.

other parameters, such as the depth and width, to study solitary wave production.

The main problem with describing solitary waves is the danger of mistaking linear Airy waves for solitary wave-type disturbances. There are a number of criteria that are unique and distinctive to solitary waves. Firstly, solitary waves must maintain their amplitude as they propagate, a property known since the time of Russell. Secondly, no asymmetries should develop in the wave. Thirdly, the wavelengths of linear dispersive waves would increase with time, contrary to solitary waves which would maintain their wavelength, and finally, periodic solitary wave emission is associated with a dispersive wave train following the disturbance (Moreira et al., 2014), known as proto-solitons or precursor solitary waves. The difference between solitary waves and linear waves are studied experimentally by Fourdrinoy et al. (2020), where all the aforementioned criteria are described. Thus, the solitary waves described by Ertekin et al. (1984a) at $F_h = 0.8$ (and lower speeds by Huang et al. (1982)), which decay with distance do not fit the *modus operandi* of solitary waves and are more likely a linear dispersive phenomenon.

Recent contributions to the field of ship-generated solitary waves and disturbance propagation at the critical depth Froude number include the work of Choi et al. (1991). They modelled the aforementioned scenario using a pressure patch to represent a series 60 ship, employing the KP approach discussed previously alongside a nonlinear Finite Element-based approach. Choi et al. (1991) showed some disagreement between results at $F_h = 1.1$ which decreased and were not significant at lower depth Froude numbers. They interpreted this through the lack of non-linear terms in the KP approach. Similarly, Chen and Sharma (1995) used the KP approach to model three dimensional waves produced at $F_H = 1$. While the authors mention their method is

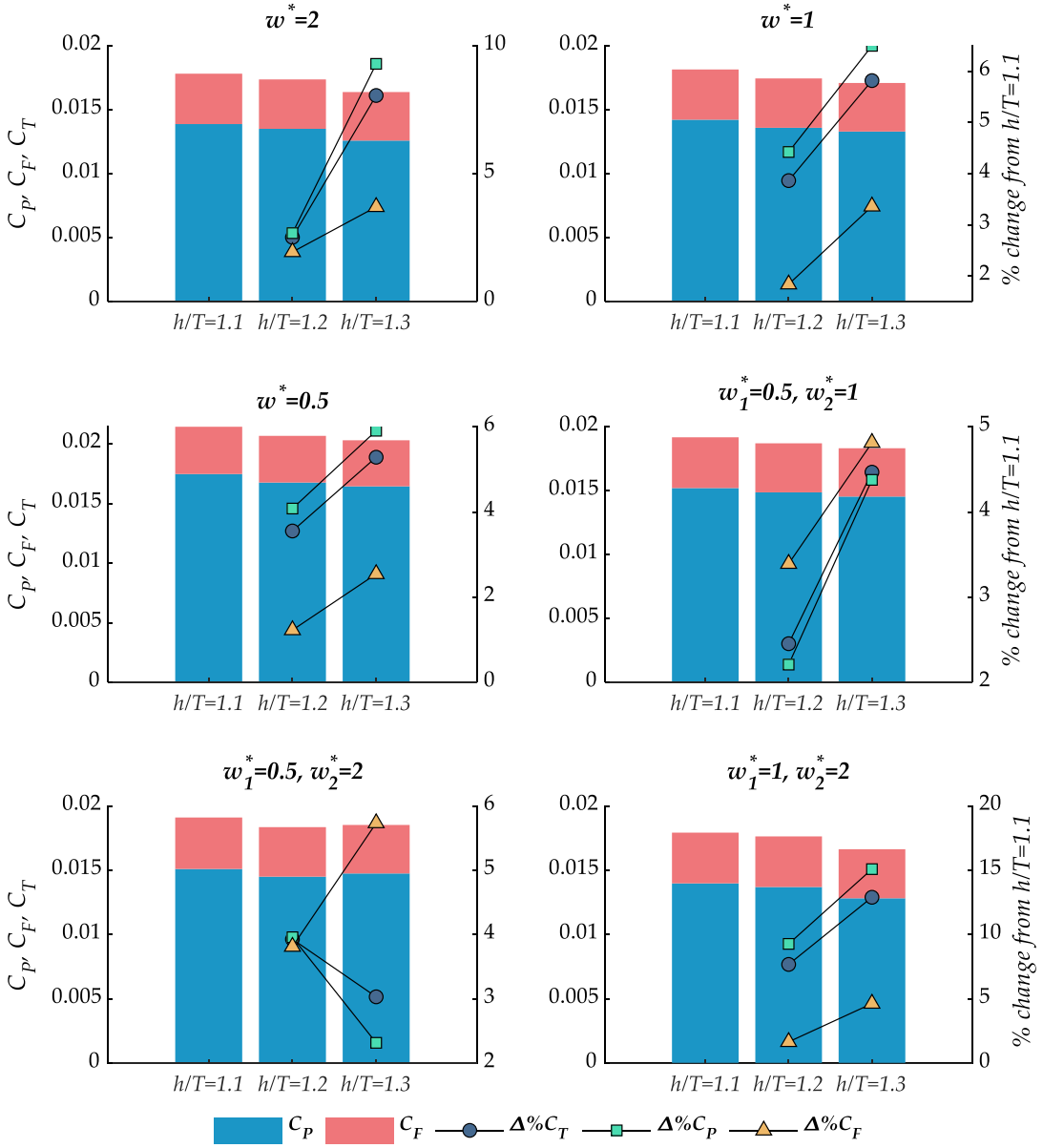

Fig. 5. Average resistance coefficients and % change relative to $h/T = 1.1$. Note: $C_T$is the sum of C_F and C_P.

not restricted to the investigated symmetrical conditions, they do not show the effect of asymmetry. The present study will fill this gap.

Li and Sclavounos (2002) modelled three-dimensional non-linear ship-generated solitary wave propagation using potential theory. Their key finding is that speeds higher than $F_h = 1$, parabolic solitary waves are formed ahead of the ship which are not able to escape upstream. The results of Li and Sclavounos (2002) show a key limitation of URANS-based approaches: timeframes up to 1200s are shown to be minimum requirements for the upstream disturbance to propagate a few body lengths. The computational demands of URANS solvers would make such modelling prohibitively expensive. It is therefore worthwhile to establish the extent to which URANS approaches are suitable for the modelling of ship-generated solitary waves. The most recent study on ship-generated solitary waves is by Alam and Mei (2008) who modelled the effects of a randomly uneven seabed. They showed that seabed undulations reduce the continuous radiation of solitary waves to a steady mass of water which is pushed upstream by the ship.

From a practical viewpoint, the energy required to emit a solitary wave must come from a ship's powerplant. Previous research shows that resistance increases exponentially near $F_h = 1$ (Terziev et al., 2023a). Better understanding of the phenomena occurring at such speeds and their impact on the total resistance rather than the predominantly modelled wave resistance is important. Although it is unlikely that many ships have the necessary installed power to reach such depth Froude numbers, several examples of highly energetic events that cause damage to the environment have been recorded across the world (Bellafiore et al., 2018; Muscalus and Haas, 2022; Torsvik et al., 2009). In addition, where confinement level is high (high blockage ratio), solitary waves can be emitted at what are considered to be low speeds. In the UK context, it can be shown that such highly energetic events may occur at speeds as low as 4mph due to the highly sedimented nature of many of the artificially constructed inland waterways (Terziev et al., 2023b). It should also be considered that solitary wave emission is not restricted to cases where the speed is maintained at $F_h = 1$. Several studies have demonstrated that solitary waves can be emitted by a ship advancing over depth changes in the waterway (Grue, 2017; Jiang, 1999; Li et al., 2023; Terziev et al., 2020).

The present study aims to investigate the effects of depth and width on solitary waves produced by a vessel operating at the critical speed through Unsteady Reynolds Averaged Navier-Stokes (URANS)

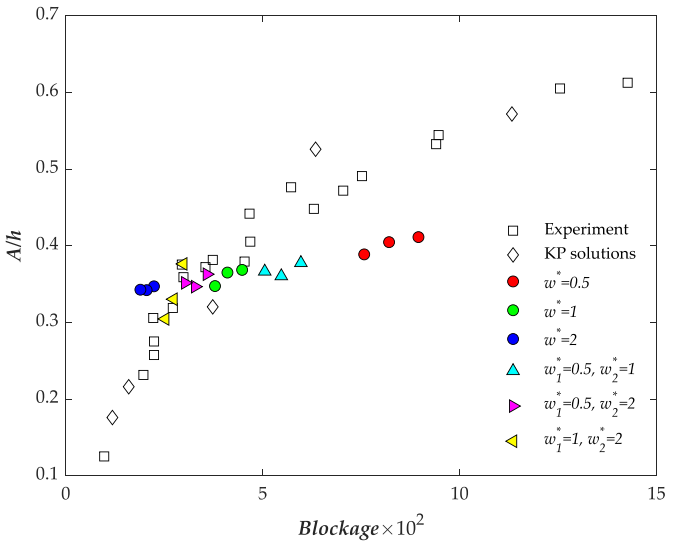

(a) Dimensionless solitary wave amplitude

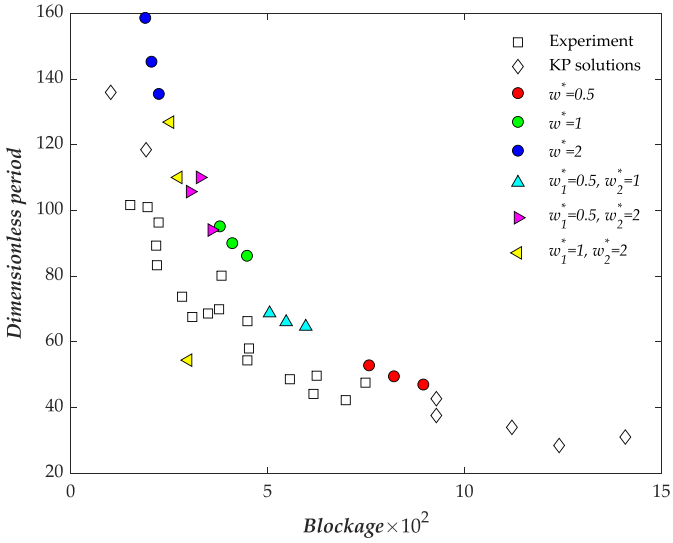

(b) Dimensionless solitary wave period (TU/h)

Fig. 6. (a) Comparison of the solitary wave amplitude, made dimensionless using the water depth versus the blockage; (b) comparison of the solitary wave dimensionless period ($\boldsymbol{TU/h}$) versus blockage. Empty shapes show data taken from Katsis and Akylas (1987). All data points are shown in triplets corresponding to the cases where $\boldsymbol{h/T}$=1.3, 1.2, and 1.1 from left to right.

modelling. Although numerous studies are devoted to ship performance at low speeds, to the best of the authors' knowledge, ship-generated upstream advancing waves have not previously been investigated using a URANS approach. That is the key gap in the literature the present paper aims to fill, in addition to re-invigorating research in this area through fully non-linear, three-dimensional numerical models while contributing to the understanding of the conditions under which upstream disturbances can be generated.

A key challenge in URANS-based modelling of solitary waves is dealing with the shelf of water typically found to accumulate upstream of the ship when waves are generated. In fact, the trough of the upstream waves typically lies above the undisturbed water level (Lee and Grimshaw, 1990), which means the ship is pushing a mass of water upstream. Due to the finite extent of computational domains, that shelf will eventually reach the inlet boundary causing unphysical effects which would not be observed in reality. For this reason, a special arrangement of boundary conditions is presented subsequently which are demonstrated to be successful in handling the above problem.

3. Case studies

The Wigley hull is used throughout the present study to maximise the ability of other researchers to re-use the results presented subsequently. The principal dimensions of the hull form used are shown in Table 1.

As explained previously, solitary waves are emitted at $F_h = 1$ regardless of the water depth and width. However, it is interesting to explore the effect of depth on the resistance experienced by the hull in addition to the properties of the solitary waves for varying depths and widths. As mentioned in Section 2, Mei (1986) found that solitary waves are produced even when the waterway is larger than one ship length. As computational domains are typically assumed infinitely wide when the half-width is two ship lengths, such a condition is included in the case study matrix. In addition, the width is halved twice to gauge the effect of lateral confinement. The resulting dimensionless half-widths ($w^* = w/L = 2, 1, 0.5$) are combined with depth-to-draft ratios $h/T = 1.1, 1.2$ and 1.3 to gauge the effect of depth (Fig. 1).

Finally, the present paper aims to test the two-dimensional nature of solitary wave by introducing an asymmetry at their inception point – the ship bow. This is achieved through bank effects, which create uneven flow in the space between the hull and asymmetrically placed boundaries relative to the ship track. Thus, the flow has a higher velocity on one side of the ship. The full test matrix is given in Table 2.

4. Numerical set up

The URANS simulations are conducted using the commercially available solver Star-CCM+, version 17.04.008-r8. The solver makes use of the finite volume method to split the computational domain into a finite number of adjoining cells. Sinkage and trim are not modelled to simplify the problem at hand.

The Volume of Fluid method is used to model the free surface (Hirt and Nichols, 1981) with High Resolution Interface Capturing (HRIC) to improve the resolution of the solution. All discretisation terms are set to second-order accuracy except the discretisation of the temporal term, which is maintained at 1st order to prevent placing excessive limits on the time step, namely, the Courant number is maintained below 1 on the water surface.

The time step varies according to the case study examined. In all cases, the time step is calculated as $\Delta t = 0.0035L/V$. It should be noted that the equation for Δt has been shown by several studies to be an adequate choice in confined water ship hydrodynamics (Campbell et al., 2022; Terziev et al., 2021).

All simulations carried out in the present study make use of the standard k-ω (Wilcox, 2008) turbulence model based on its ability to solve similar case studies faster than other 2-equation eddy-viscosity turbulence models with similar accuracy (Terziev et al., 2019).

4.1. Computational domain and boundary conditions

The computational domain consists of a rectangular box, extending four ship lengths downstream of the aft perpendicular and four ship lengths upstream of the forward perpendicular, where a pressure outlet and velocity inlet are implemented, respectively. Vertically in the positive z direction the domain extends one ship length from the undisturbed water level, where a velocity inlet is instituted. The domain sides, bottom, and ship hull are no-slip wall boundaries. In addition, a symmetry plane is used to bisect the domain and half the required cell numbers because, as discussed previously, solitary waves show no variation in the y direction in symmetrical conditions marked with an asterisk in Table 2. Asymmetrical cases do not make use of a symmetry boundary condition.

To guarantee that upstream disturbances are eliminated before they

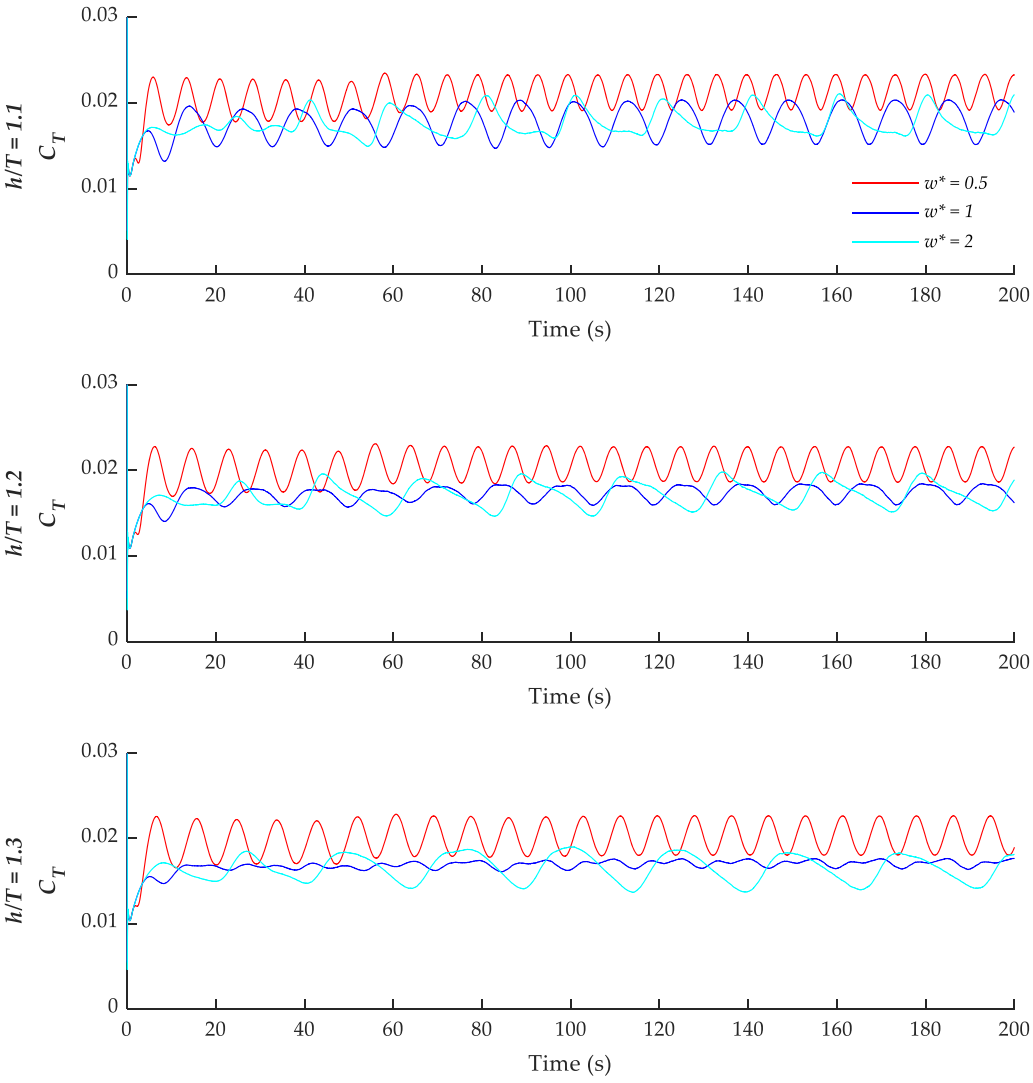

Fig. 7. Time-history of the total resistance coefficient in the symmetrical cases.

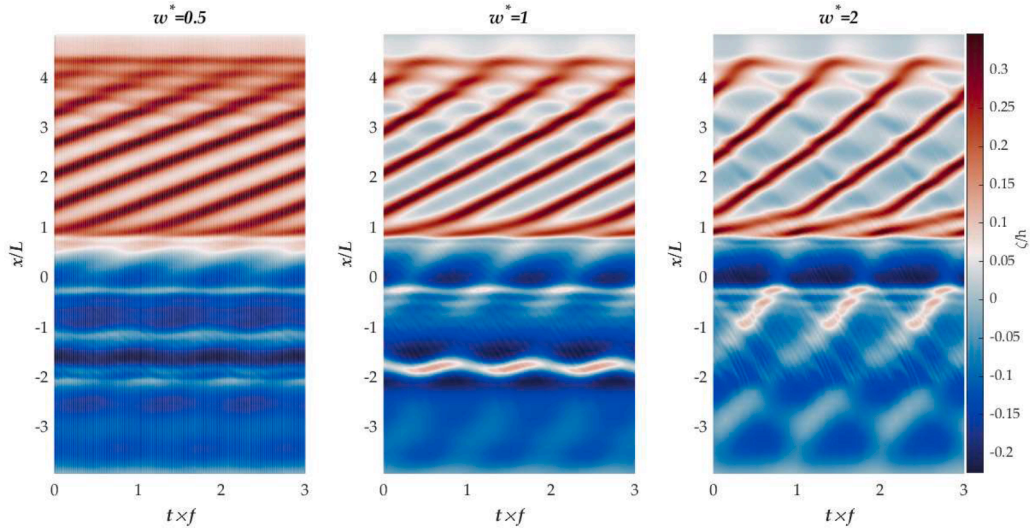

Fig. 8. Time-history (where t is time and f is the frequency of the oscillation of the total resistance coefficient for each case) of the free surface elevation along $w^* = 0.1$ over the last three oscillation cycles of the total resistance coefficient. The hull is located between $0 < x/L < 1$. The conditions depicted correspond to $h/T = 1.1$.

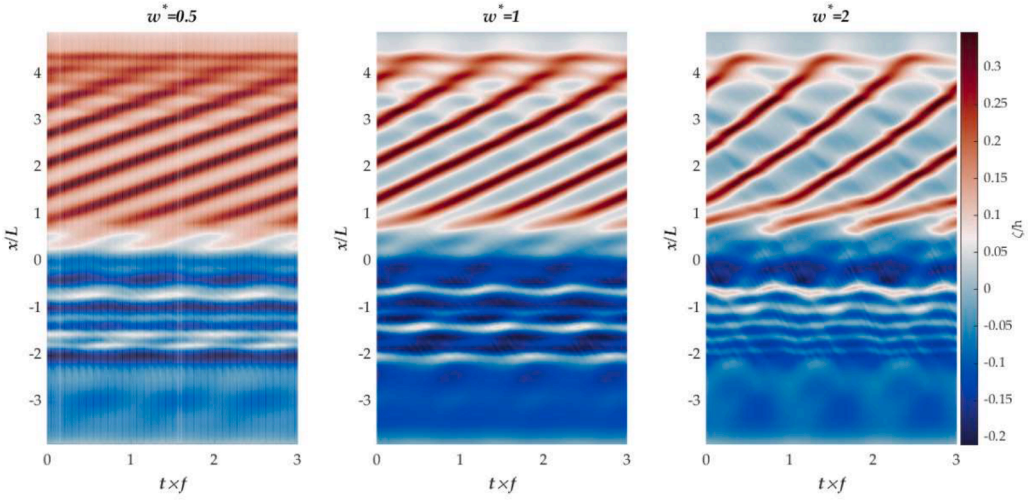

Fig. 9. Time-history (where t is time and f is the frequency of the oscillation of the total resistance coefficient for each case) of the free surface elevation along $w^* = 0.5$ over the last three oscillation cycles of the total resistance coefficient. The hull is located between $0 < x/L < 1$. The conditions depicted correspond to $h/T = 1.1$.

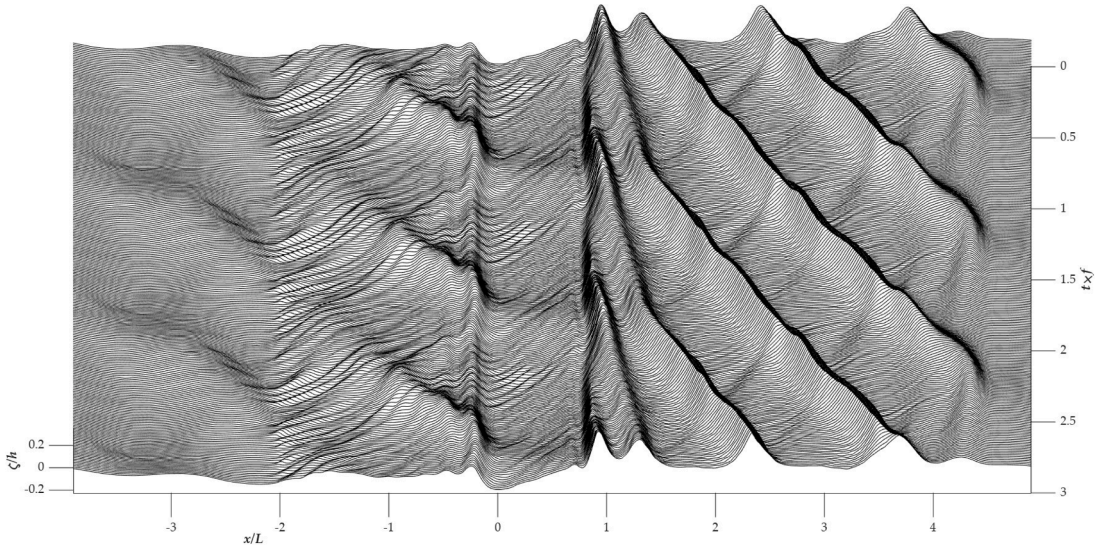

Fig. 10. Three cycles of solitary wave generation and upstream propagation for $h/T = 1.1$, $w^* = 2$. The wavecut shown is located at $w^* = 0.1$. The hull is located between $0 < x/L < 1$ and indicated by a dotted line.

reach the inlet, the domain is extended a further half ship length where the bottom boundary condition is different: The area spanning $-4L$ to $4L$ is a no-slip wall as stated previously. However, the area between $4.5L$ and $5L$, where the inlet is located, the boundary condition is switched to a pressure outlet. The pressure outlet maintains the hydrostatic pressure and prevents the build-up of the shelf of elevated water. Through a process of trial and error, it was found that half ship length starting at the inlet is sufficient to eliminate disturbances. In addition, wave damping is imposed on the inlet and outlet covering a distance of 1 ship length in the boundary-normal direction. The computational domain is depicted in Fig. 2.

4.2. Computational mesh

The unstructured computational mesh is designed within the automatic facilities of the employed solver. Flow-aligned hexahedral cells are distributed throughout the domain. The meshing strategy consists of a set of concentric refinements to capture the location of the Kelvin waves in addition to an upstream refinement created to target the radiation of ship waves. That refinement extends 4.5 times the ship length upstream of the forward perpendicular, with the mesh coarsening further upstream to dampen the disturbance. In addition, numerical damping, extending one ship length in the boundary-normal direction is implemented at the inlet and outlet.

4.2.1. Near-wall modelling strategy

The near-wall modelling strategy is to maintain a $y^+ > 30$ over the surface of the ship, while the domain bottom and sides are set to maintain $y^+ < 1$. The ship near-wall layers are determined through the approach exemplified by Terziev et al. (2022). Namely, the frictional resistance coefficient is determined through the ITTC correlation line.

$$C_f = \frac{0.075}{(\log_{10} Re - 2)^2} \tag{2}$$

where $Re = VL\mu/\rho$ is the Reynolds number with μ being the dynamic viscosity of water and $\rho = 998.561$ kg/m^3. Once the value of C_f is known, the friction velocity is predicted as $u_\tau = \sqrt{\tau_w/\rho}$, with $\tau_w =$

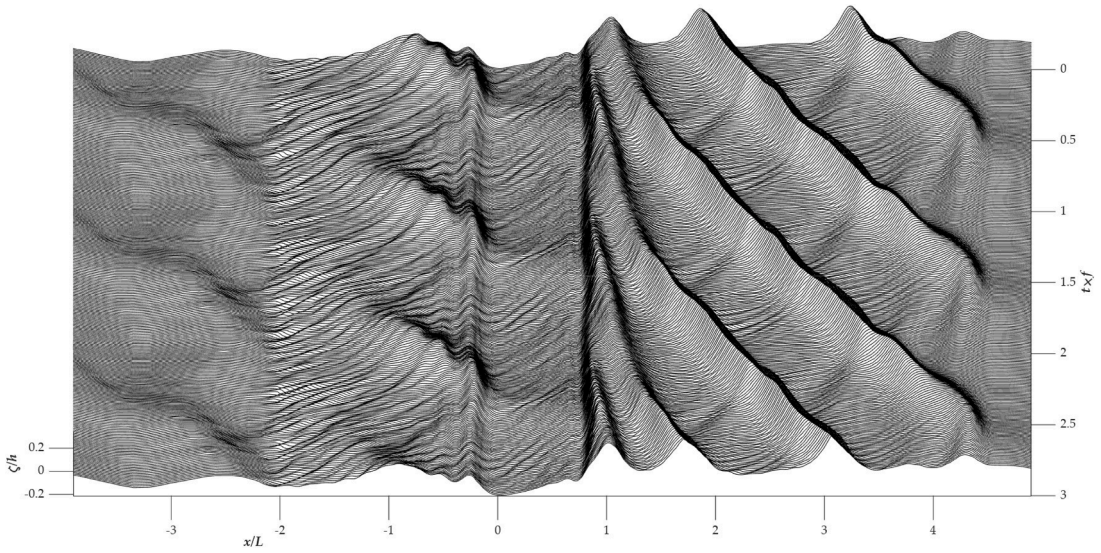

Fig. 11. Three cycles of solitary wave generation and upstream propagation for $h/T = 1.2$, $w^* = 2$. The wavecut shown is located at $w^* = 0.1$. The hull is located between $0 < x/L < 1$ and indicated by a dotted line.

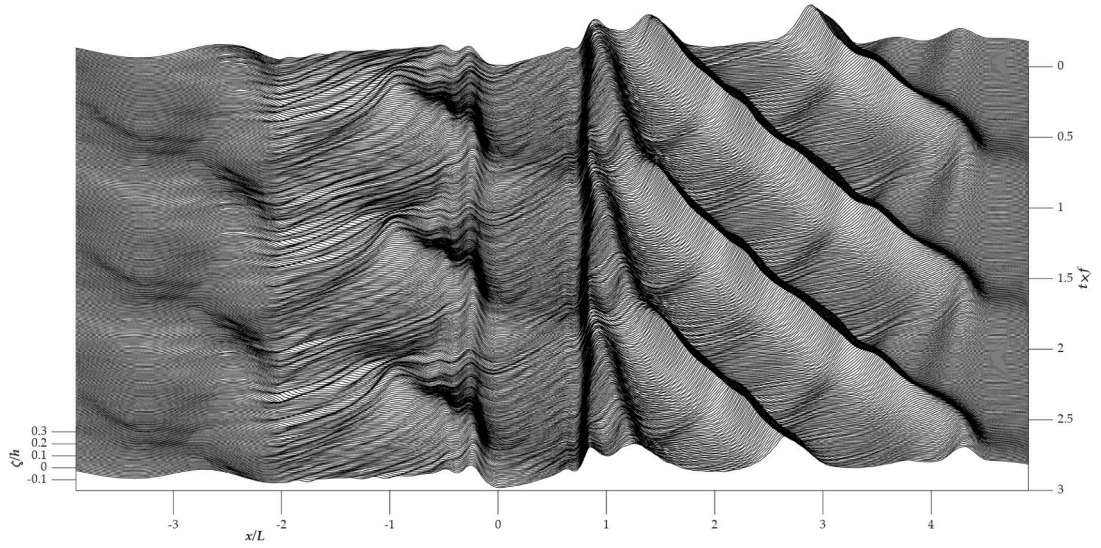

Fig. 12. Three cycles of solitary wave generation and upstream propagation for $h/T = 1.3$, $w^* = 2$. The wavecut shown is located at $w^* = 0.1$. The hull is located between $0 < x/L < 1$ and indicated by a dotted line.

$0.5C_f\rho V^2$, which gives the first layer thickness $\Delta y = y^+_{target}\nu/u_\tau$, where $\nu = \mu/\rho$. The value of y^+_{target} is set to 150 giving a margin to account for the level of confinement being modelled. The number of near-wall layers (n) is then predicted as shown in Eq. (3):

$$n = \log(-\delta(1-S)/(2\Delta y+1))/\log(S) \tag{3}$$

where δ is a fraction of the flat plate equivalent boundary layer thickness, $0.382L/Re^{1/5}$, and S is the ratio of the thickness of any two adjacent layers. The resulting mesh is depicted in Fig. 3, which consists of approximately 4.9 million cells for case 2 ($h/T = 1.1$, $w^*_1 = 1$ $w^*_2 = 2$) and 3.7 million cells for case 13, for example ($h/T = 1.3$, $w^* = 2$).

5. Results and discussion

The first item to be investigated is the resistance of the Wigley hull under the conditions examined. Pressure resistance (R_P), frictional resistance (R_F), and total resistance (R_T) are made dimensionless through dividing by $0.5SV^2\rho$ in all cases, where $S = 1.338$ m^2 (C_P, C_F, and C_T, respectively). In all symmetrical cases, the predicted resistance values are doubled to show the resistance for the entire body.

5.1. Resistance coefficients

The frequency of oscillation and amplitude of the total resistance are extracted for each case examined using a Fast Fourier Transform (FFT) approach and given in Fig. 4. The frequency of oscillation generally shows a monotonic decrease across all case studies investigated. This is particularly visible when the width is large. The CFD model suggests that a reduction in frequency with increases in water depth is reproduced across all case studies, mirroring the experimental results of Ertekin et al. (1984b) who presented similar results against blockage. When the width is large, the water depth has a relatively weak effect on the frequency and amplitude of oscillation. For example, when $w^* = 2$, the frequency decreases with increasing water depth from 0.05 Hz to 0.045 Hz and 0.04 Hz when $h/T = 1.1$, 1.2 and 1.3, respectively. The

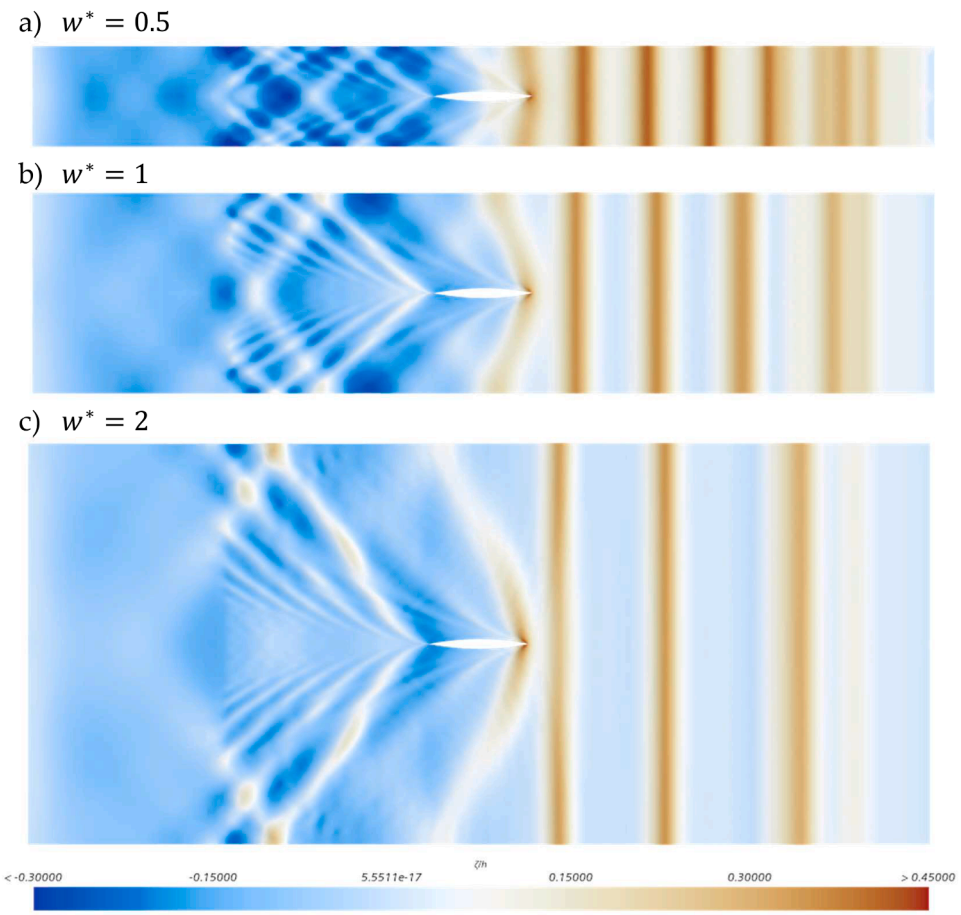

Fig. 13. Instantaneous snapshots of the free surface at a time $t = 300$ s for the symmetrical cases at $h/T = 1.1$.

introduction of asymmetry appears to affect the results considerably. Specifically, when $w_1^* = 1$, $w_2^* = 2$ the frequency reduces from 0.13 Hz to 0.06 Hz and 0.05 Hz when $h/T = 1.1$, 1.2 and 1.3, respectively.

The amplitude of oscillation is affected by the water depth in a more complex fashion than the oscillation frequency. As was the case for frequency, the amplitude is weakly dependent on the water depth provided the width is sufficiently large; for example, the amplitude decreases by approximately 1 % when $w^* = 2$. Reductions in the width of the domain and introduction of asymmetry show a highly complex interaction with the amplitude of oscillation. The results point to a particular width that causes enhanced oscillations. These effects may be explained using the wave field and more specifically, reflections of waves from the domain sides and their interactions with the ship stern, explored subsequently.

A consequence of the majority of analysis methods relying on inviscid flow is that the effects of friction and pressure have not previously been examined in a fully nonlinear viscous framework. The present sub-section aims to fill this gap.

Fig. 5 shows that resistance is strongly dependent on the restriction as well as on the water depth. In all cases, $w^* = 0.5$ shows the highest resistance value. The total resistance coefficient when $w_1^* = 0.5$, $w_2^* = 2$ shows the second highest values for $h/T = 1.1$ and $h/T = 1.2$, but not for $h/T = 1.3$, where the second highest resistance was recorded when $w_1^* = 0.5$, $w_2^* = 1$.

The effect of water depth may also be quantified through the average resistance coefficients for the same case, shown in Fig. 5. Namely, for the symmetrical cases, reducing the water depth has the largest effect when $w^* = 2$, reducing all resistance coefficient by between 2.68 % and 1.94 % when $h/T = 1.2$ relative to $h/T = 1.1$. On the other hand, the relative difference between $h/T = 1.2$ and $h/T = 1.3$ is considerably higher and shows a strong sensitivity to the coefficient examined. Specifically, C_F reduces by only 3.7 %, while pressure and total resistance drop by approximately 8 % and 9.3 % respectively. The remaining symmetrical cases, $w^* = 1$ and $w^* = 0.5$ show relatively similar reductions with increasing water depth of no more than approximately 6 %. In these cases, the friction and pressure resistance coefficients show less significant reduction.

The effect of water depth is more complicated when asymmetry is introduced. To begin with, Fig. 5 shows that friction can account for the main source of change due to water depth, contrary to expectation when $w_1^* = 0.5$, $w_2^* = 1$ of approximately 4.8 %. For the same case, pressure and total resistance reduces by 4.38 % and 4.47 %, respectively. A similar pattern can be observed for $w_1^* = 0.5$, $w_2^* = 2$, where the contribution due to friction reduces by 5.7 % while the pressure resistance reduces by 2.3 %. Since pressure resistance is the dominant contributor to the total, C_T is reduced by only 3 % in this case. Water depth has the strongest effect when $w_1^* = 1$, $w_2^* = 2$, where the pressure resistance coefficient may reduce by up to 15 % from $h/T = 1.1$ to $h/T = 1.3$. Due to the comparatively smaller change in the frictional resistance coefficient, the total resistance coefficient reduces by 12.9 %.

The constituent components of the total resistance coefficient shown in Fig. 5 justify the use of inviscid methods because pressure resistance components dominate the total resistance in all cases. It is however interesting to examine changes in relative contributions. For example, the pressure resistance coefficient accounts for 81.52 % of the total resistance coefficient when $w^* = 0.5$ for $h/T = 1.1$, showing a marginal reduction with increases in depth to 80.98 %. Similarly, C_P accounts for 76.84 % when $w^* = 2$ for $h/T = 1.3$, only 1 % less than when $h/T = 1.1$. Variations of less than 1 % may be observed when $w_1^* = 0.5$, $w_2^* = 2$, indicating a stable distribution in the relative magnitude of the two

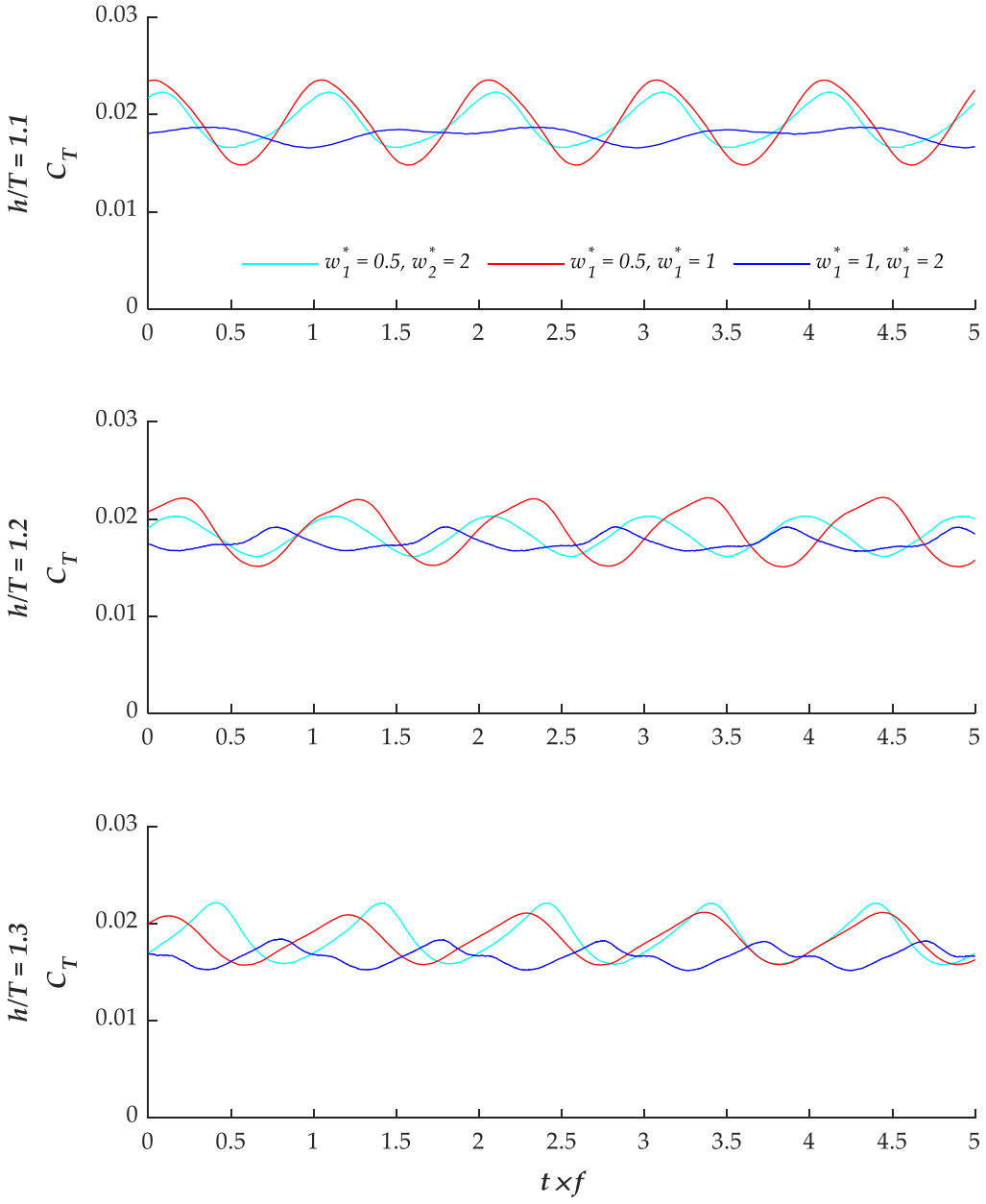

Fig. 14. Time-history of the total resistance coefficient for all asymmetrical cases over five solitary wave shedding cycles.

main sources of resistance.

Having compared the properties of the resistance coefficients, it is also instructive to determine the agreement between the present CFD model and existing experiments. For this purpose, results compiled by Katsis and Akylas (1987) which include theoretical and experimental data are used. The comparison depicted in Fig. 6 demonstrates that the present CFD-obtained solitary wave amplitudes exhibit good agreement throughout the high blockage ratio range, which is more challenging to capture from a computational point of view. Similarly, the dimensionless period shows excellent agreement with experimental and theoretical data. It can therefore be concluded that the present CFD model has modelled the properties of the upstream-emitted waves accurately. In all cases, wave properties were measured as close to the ship centreline as possible. This may explain some of the small disagreement shown in Fig. 6.

5.2. Ship-generated solitary waves in symmetrical conditions

Fig. 7 shows the time history of the total resistance coefficient in the symmetrical cases. In all cases, the resistance oscillates. In the highly restricted case, $w^* = 0.5$, the oscillation is near-sinusoidal, while the pattern becomes more complex with increases in w^*. The observed

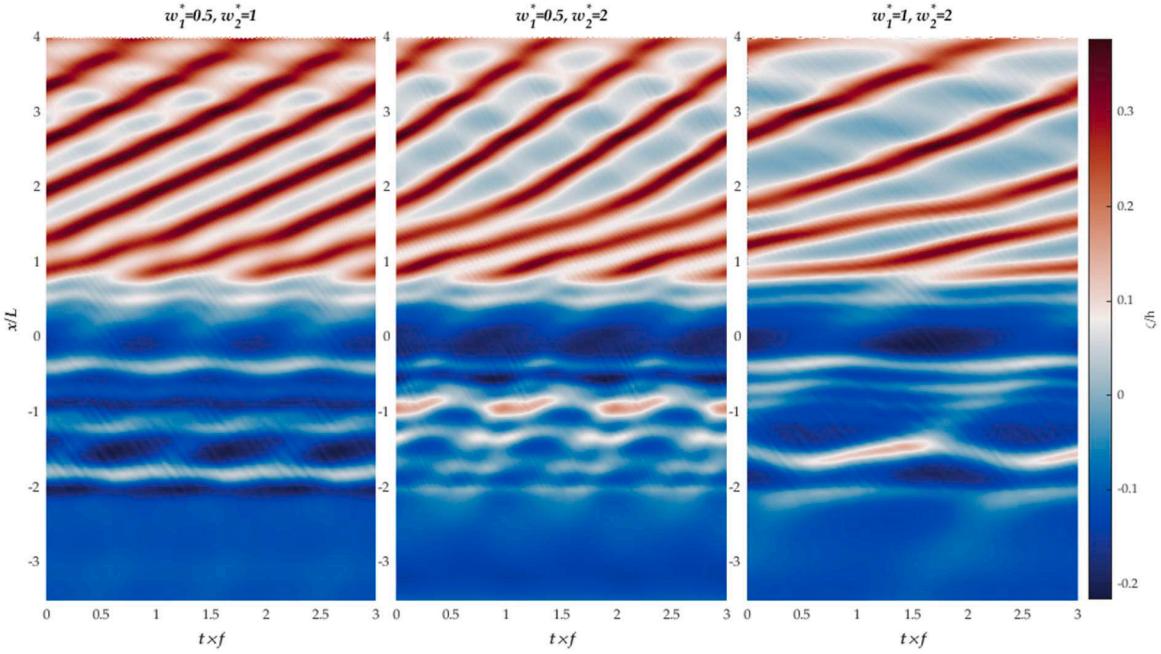

Fig. 15. Time-history (where t is time and f is the frequency of the oscillation of the total resistance coefficient for each case) of the free surface elevation along $w^* = 0.2$ over the last three oscillation cycles of the total resistance coefficient. The hull is located between $0 < x/L < 1$. The conditions depicted correspond to $h/T = 1.1$.

differences are found to originate in the manner in which the solitary wave builds before it is able to create a sufficient change in the local water depth to bypass the wave speed, $\sqrt{gh}$.

If the domain width is small, e.g. $w^* = 0.5$, the process described previously is relatively quick and allows only weak reflections from the domain side to propagate aft in a diamond shape. However, when the domain width is sufficient, wave reflections from the boundary can increase in magnitude and are detectable aft of the vessel as shown in Figs. 8 and 9. In addition, the speed at which the solitary wave advances shows a sharp change at $t \times f = 1,\ 2$ when $w^* = 1$ and $w^* = 2$ due to the aforementioned phenomenon. It is at that point that the entire distance from the ship centreline to the domain side has achieved a uniform distribution in height (and therefore energy) and is able to escape upstream at a uniform speed as a two-dimensional disturbance.

The delay in solitary wave emission resulting from the process of distributing energy along the domain width reduces the frequency of solitary wave generation. This explains why the level of confinement is a key determinant in the frequency, but influences the height of solitary waves weakly , since in all cases the waves propagate at a local modified speed. In addition, the above observation explains the shape of the time-history of the total resistance. The delay in emission of the solitary wave causes the wave to initially detach at a lower speed while energy is transferred along the canal width and is responsible for the slope of the C_T curve shown in the time-history when $w^* = 2$ (see Fig. 7).

The reflection of the solitary wave at the canal side as the height builds up creates an oscillation in the water level aft of the hull, as shown in Fig. 10. At the beginning of each solitary wave shedding cycle, the wave generated at the bow is of low amplitude and reflects from the canal side at a distance of more than one ship length as recorded by a wavecut located at $w^* = 0.1$. As energy is distributed from the bow along the width of the solitary wave, the local water depth is modified causing an increase in the speed of the reflected component which catches up with the ship at $x/L = 1$ at the point when the entire system has achieved sufficient elevation to escape upstream.

Figs. 10–12 also show the success of the computational domain boundary conditions imposed. Specifically, the pressure outlet which replaces the domain bottom no-slip wall condition between $4L$ and $4.5L$ successfully prevents reflections of the solitary wave as they reach the inlet boundary. To support the above claim, Fig. 13 shows the destruction of the upstream disturbance for all widths prior to the domain inlet. In addition, Fig. 13 demonstrates that the mean water level is successfully reduced to the mean ζ/h=0.

5.3. Ship-generated solitary waves in asymmetrical conditions

As was the case for the symmetrical cases, a single oscillation frequency corresponding to the shedding cycle of solitary waves dominates the total resistance coefficient, shown in Fig. 14. Increases in water depth cause a reduction in the oscillation amplitude and morph the shape of the time-history into a sawtooth shape. In addition, case 14 ($h/T = 1.3$, $w_1^* = 1,\ w_2^* = 2$) exhibits a secondary frequency produced by the asymmetry of the case studies, as examined subsequently.

The periodic disturbances aft of the hull are in all cases stronger when the ship and canal centreline do not coincide. Reinforcements and cancellations in the wake pattern are distinct from the symmetrical cases because components of the bow and stern wave systems travel over varying distances port and starboard to reflect. This creates a complex wave pattern aft of the hull, as shown in Figs. 15 and 16.

Fig. 16 also shows that side boundary distances to the ship centreline are key in the frequency of emitted solitary waves. By contrast to the symmetrical cases, when asymmetry is introduced, the shape of the upstream emitted solitary wave shows some dependence on the width.

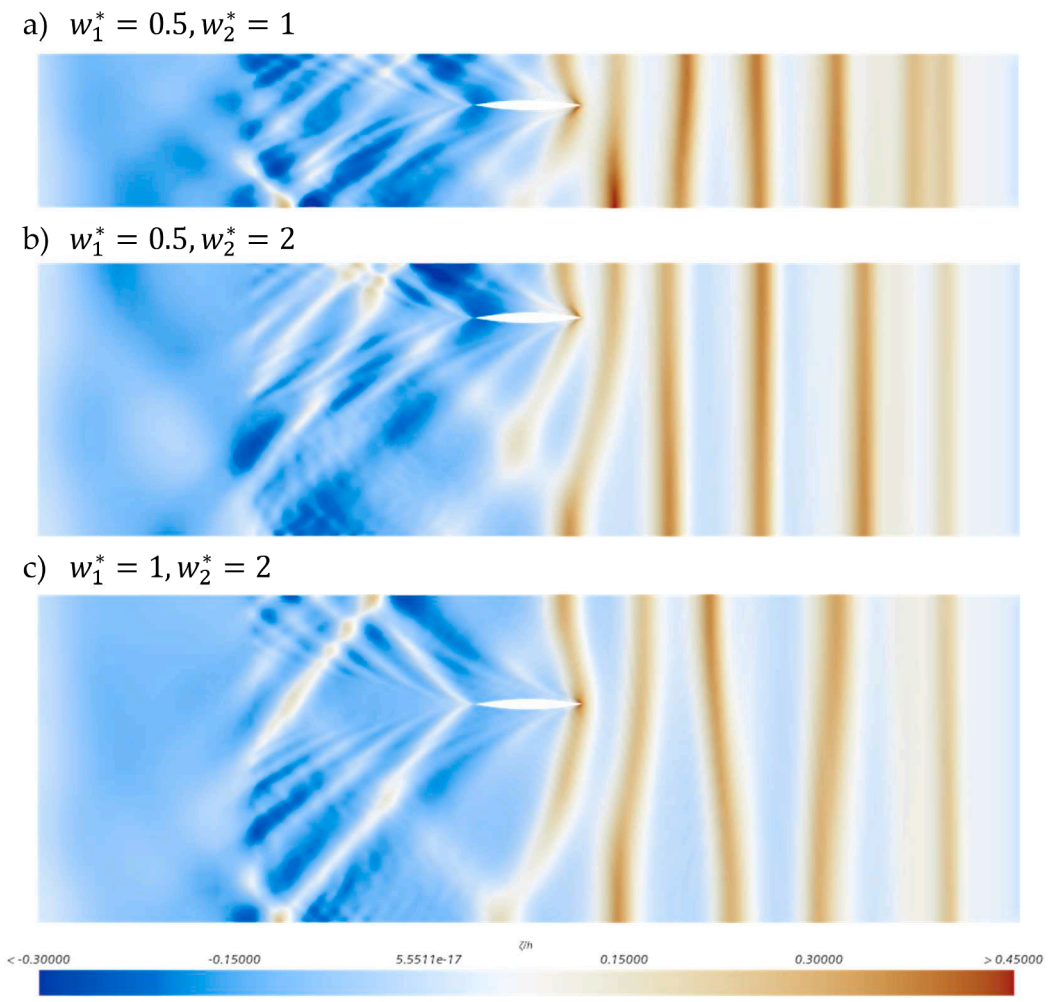

Fig. 16. Instantaneous wave patterns at $t = 300$ s produced by the hull in varying asymmetrical conditions when $h/T = 1.1$.

Specifically, the solitary wave achieves the necessary height to escape upstream on the port side before it does so on the starboard side. Energy is then distributed across the wave width, as was the case in the symmetrical cases. However, the degree of asymmetry introduced in the present section is sufficient to prevent the perfect 2D behaviour immediately upstream. For this reason, solitary waves are seen to distribute energy across their width not only at the point of their inception, but also as they propagate upstream.

When asymmetry is small, e.g. $w_1^* = 0.5$, $w_2^* = 1$, solitary waves quickly achieve their 2D shape, but when $w_1^* = 1$, $w_2^* = 2$ it can be observed that too much energy is distributed to one side. Typically, this causes the port end of the solitary wave to advance faster than the starboard side, which is then corrected causing the starboard side to overtake the remainder of the wave. The difference between the wave elevation port and starboard at $w^* = 0.4$ is shown in Fig. 17. The figure shows a period change from positive to negative $\Delta\zeta = \zeta_{w_1^*} - \zeta_{w_2^*}$ values, which peak when $w_1^* = 0.5$, $w_2^* = 2$. The reason for this consequence is the effect of the near-field disturbance, which as shown in Fig. 16, extends from the hull to the domain side.

5.4. Sway force and yaw moment

Due to the asymmetry of the examined case studies, one expects to observe the effect of solitary wave shedding on the time-history of the sway force and yaw moment. The former is made dimensionless (C_S) in the same way as the total resistance coefficient, while an additional term (the ship length) is added in the denominator to ensure consistency of the units of the yaw moment coefficient (C_Y). A standard right-handed coordinate system is employed, which rests amidships.

Two general observations can be made from the time-history of the sway force coefficient shown in Fig. 18. Firstly, increasing the water depth reduces the amplitude of oscillation in C_S. Secondly, the mean value of the sway force coefficient is closer to the 0 point when the depth is larger. When the waterway is restricted, the ship experiences periodic attraction and repulsion to the side boundary. The latter being a maximum of 3.5 times larger than the former when $h/T = 1.1$ and $w_1^* = 0.5$, $w_2^* = 1$. By contrast, when $h/T = 1.3$, attraction peaks at marginally higher levels than repulsion, indicating the importance of water depth in the problem examined. Offsetting the starboard boundary (w_2^*) by a further ship length causes a shift of the sway force coefficient towards repulsion. In these conditions, the ship experiences

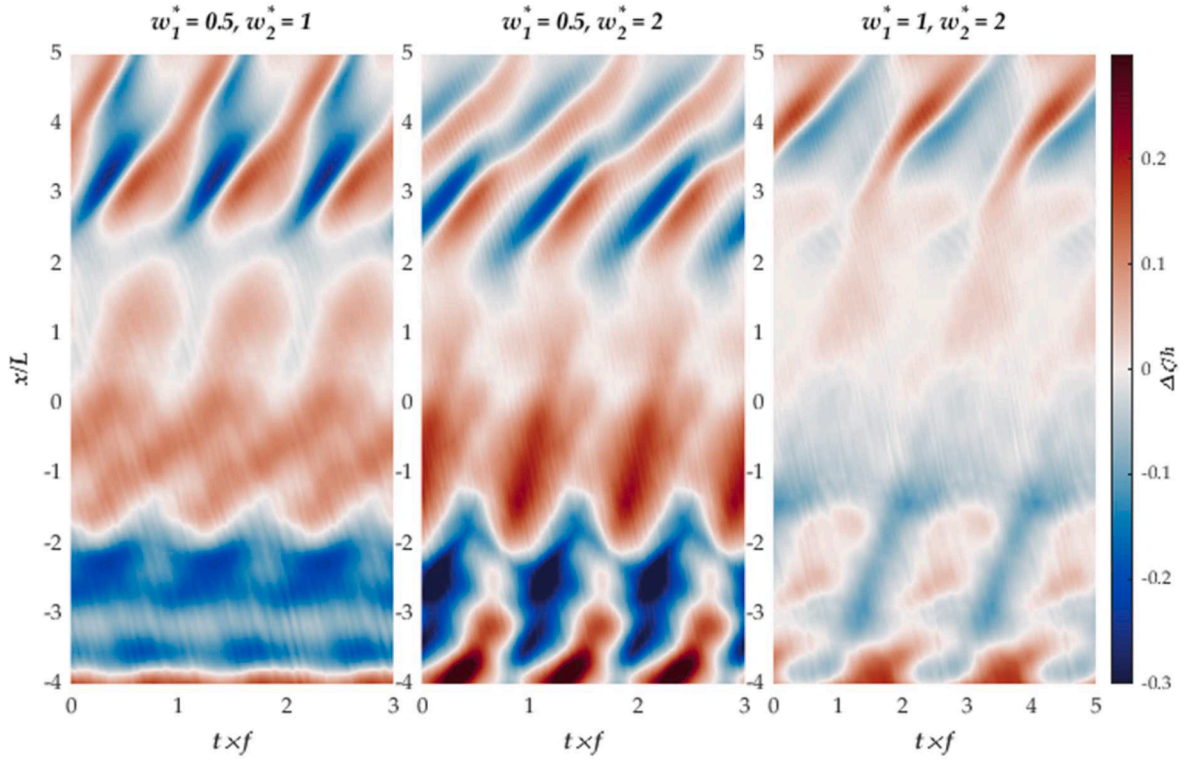

Fig. 17. Dimensionless difference in wave elevation at $w^* = 0.4$ between the port and starboard sides. Cases depicted correspond to $h/T = 1.1$.

repulsion during the majority of time, and in $h/T = 1.1$ there is solely repulsion. However, C_S values attain marginally higher absolute values when positive, in other words, the attraction peaks are once again higher than the repulsion peaks.

The yaw moment, shown in Fig. 19 also has a propensity to change sign when $w_1^* = 0.5, w_2^* = 1$, and marginally so when $w_1^* = 0.5, w_2^* = 2$ only for the smallest underkeel clearance. By contrast, when $w_1^* = 1, w_2^* = 2$ C_M oscillates considerably closer to 0. As was the case with C_S, C_M values show a preference, in this case, towards negative values corresponding to repulsion of the ship bow. Although a bow repulsive moment in experienced by the ship during the majority of a solitary wave radiation cycle, the value of attraction of the bow to the port peaks at higher values.

5.5. Verification

The mapping of the continuous form of the governing equations onto discrete intervals in time and space creates discretisation errors. That error must be estimated, typically through a technique based on Richardson Extrapolation (Richardson, 1927), which requires a minimum of two sequentially refined solutions in order to produce an estimate. The method employed here makes use of three solutions which allows the estimate of the observed order of accuracy (p), which determines the rate at which the discretisation error reduces with grid refinement:

$$p = \ln\left(\frac{\varphi_3 - \varphi_2}{\varphi_2 - \varphi_1}\right) \Big/ \ln r \tag{6}$$

where φ_k is the solution obtained using k^{th} arrangement of the computational mesh and time step, and $r = \sqrt{2}$ is the ratio of the grid/time step in any two adjacent solutions. In addition, it is convenient to define the convergence ratio, $R = (\varphi_2 - \varphi_1)/(\varphi_3 - \varphi_2)$, whose value can be used to determine the manner in which the asymptotic range is approached. For example, if $0 < R < 1$, the solution is monotonically convergent, whereas if $-1 < R < 0$, the solution exhibits oscillatory convergence.

The discretisation error can be defined as shown in Eq. (7):

$$e = \frac{\varphi_2 - \varphi_1}{r^p - 1} \tag{7}$$

which allows the calculation of the discretisation uncertainty, $U_D = 1.25E_d$, by using the Grid Convergence Index (GCI) method (Celik et al., 2008). In addition, the extrapolated solution may be defined as $\varphi_{ext} = \varphi_1 - e$. It is standard practice to magnify the discretisation error by a factor of safety (in this case 1.25) to arrive at a discretisation uncertainty.

In producing the medium (φ_2), and coarse (φ_3) solutions, the cell aspect ratio is maintained constant throughout the domain by magnifying all cells by the same refinement factor (r) (Salas, 2006). In addition, the Courant number is maintained by multiplying the time step by the same factor, as recommended by Burmester et al. (2020). Therefore, the discretisation uncertainty presented in Table 3 is the combined value of the spatial and temporal uncertainty and represents the overall numerical uncertainty.

The procedure explained in this section is applied to the properties of the total resistance coefficient. The uncertainty assessment is assumed to be representative of the full set of results used in the present study. The average magnitude of C_T is studied in addition to its oscillation frequency and amplitude. The achieved discretisation uncertainties are less

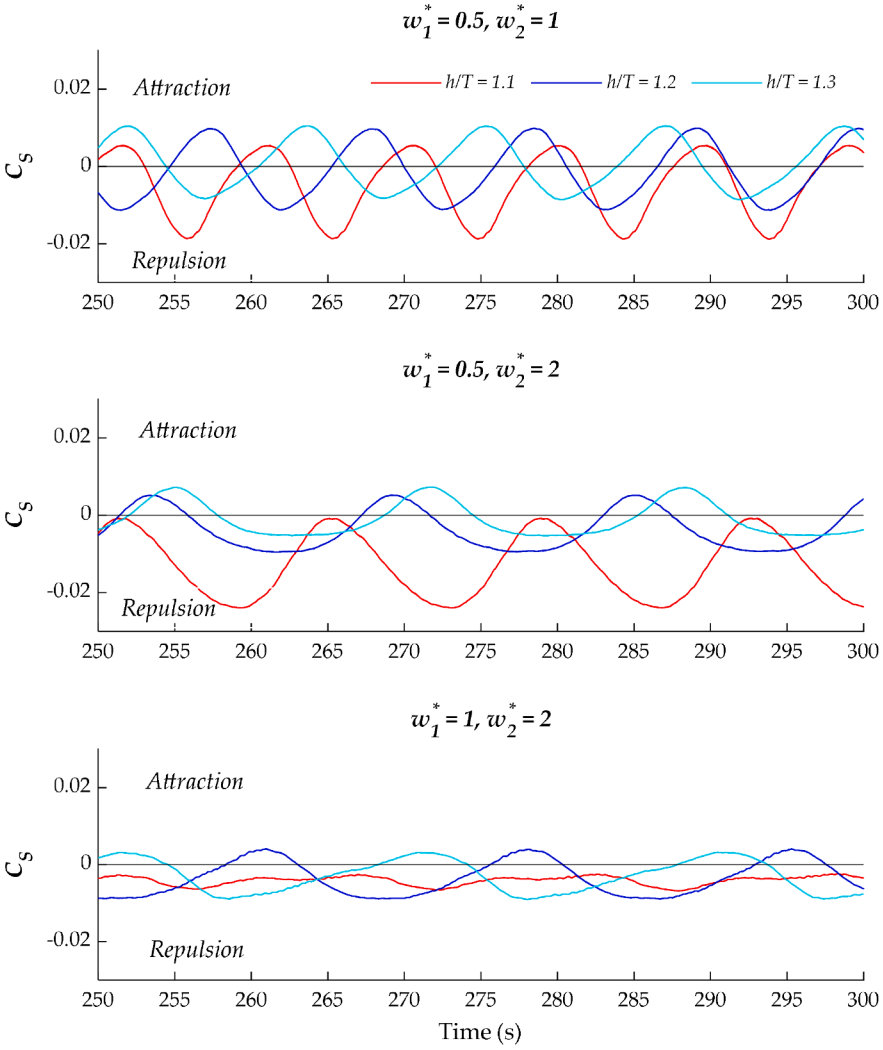

Fig. 18. Sway force coefficient for all asymmetrical cases.

than 1 % for the magnitude of C_T and its oscillation amplitude, and 2.192 % for the frequency of oscillation. The observed orders of accuracy are generally higher than the theoretical order of accuracy ($p_t = 2$), attaining values between approximately 3.5 and 6.6.

6. Conclusion

Ship-generated solitary waves have a specific set of properties which distinguishes them from typical Kelvin waves. The present study aimed at the investigation of the production and radiation of such waves under a set of varying conditions. Specifically, varying widths, from a half-width of two ship length to half ship length, and asymmetric conditions.

The present study examined the conditions causing ship-generated solitary wave radiation using a Computational Fluid Dynamics Unsteady Reynolds Averaged Navier-Stokes approach. While previous research on the topic of ship-generated solitary waves used exclusively variations of inviscid flow, to the best of the authors' knowledge, the present study is the first to employ URANS to model the problem. Crucially, the present study accounts for the effects of viscosity and is fully non-linear. The inviscid assumption is shown to be justified through the finding that frictional resistance generally accounts for more than 25 % of the total resistance coefficient, with negligible effects of water depth typically within 1 %.

The CFD model shows that changes in depth cause significant differences in the magnitude, amplitude of oscillation, and frequency of the total resistance coefficient of up to 15 % when the depth increases from $h/T = 1.1$ to $h/T = 1.3$. The frequency of oscillation in Hz decreases across all cases examined regardless of whether asymmetry is modelled or not. However, the amplitude of oscillations generally increases for highly restricted cases, when the half-width of the domain is half a ship length. Conversely, the amplitude may also decrease for cases approximating infinitely wide conditions. These results agree well with existing experimental data and data obtained using an inviscid model.

Ship-generated solitary waves are shown to dynamically distribute energy across their width. When the ship sails at the waterway centreline, solitary waves delay growth at the ship bow while sufficient energy is sent across the arms of the solitary wave until a perpendicular wave front is formed which is able to escape upstream at a uniform speed.

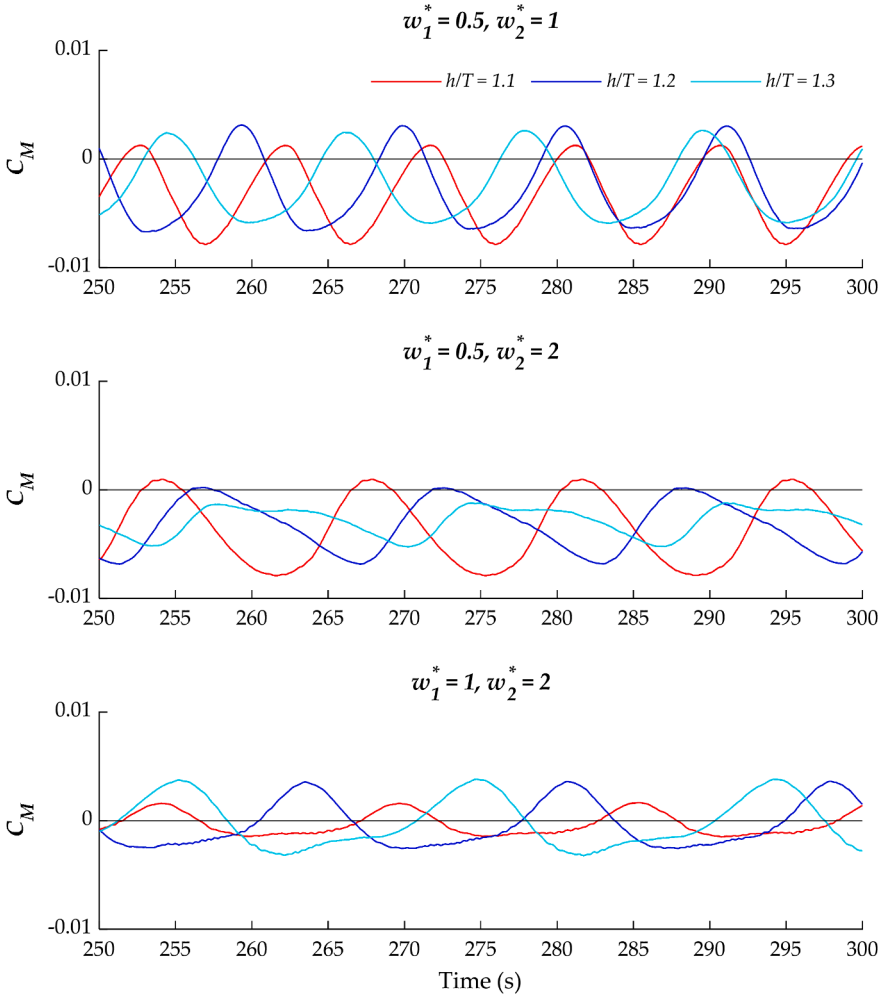

Fig. 19. Yaw moment coefficient for all asymmetrical cases.

Table 3
Results from the verification exercise applied to C_T and its properties.

Parameter	Symbol	C_T	C_T frequency	C_T amplitude
Refinement factor	r	$\sqrt{2}$	$\sqrt{2}$	$\sqrt{2}$
Fine solution	φ_1	21.417×10^{-3}	0.147 Hz	1.567×10^{-3}
Medium solution	φ_2	21.810×10^{-3}	0.158 Hz	1.638×10^{-3}
Coarse solution	φ_3	23.135×10^{-3}	0.224 Hz	2.342×10^{-3}
Convergence ratio	R	0.296	0.179	0.101
Order of accuracy	p	3.509	4.957	6.628
Extrapolated solution	φ_{ext}	21.252×10^{-3}	0.144 Hz	1.559×10^{-3}
Discretisation error	e	0.772 %	1.753 %	0.505 %
Discretisation uncertainty	U	0.966 %	2.192 %	0.631 %

When asymmetry is introduced, the same phenomenon is shown to dynamically distribute energy from port to starboard to ensure the solitary wave attains a uniform shape across the domain width. In highly asymmetric cases, energy is distributed across the solitary wave in several cycles. To the best of the authors' knowledge, the present study has been the first to model asymmetry effects in ship-generated solitary waves.

CRediT authorship contribution statement

Momchil Terziev: Conceptualization, Data curation, Formal analysis, Funding acquisition, Investigation, Methodology, Project administration, Resources, Software, Validation, Visualization, Writing – original draft, Writing – review & editing. **Atilla Incecik:** Conceptualization, Funding acquisition, Project administration, Resources, Supervision, Writing – original draft, Writing – review & editing.

Declaration of competing interest

The authors declare that they have no known competing financial interests or personal relationships that could have appeared to influence the work reported in this paper.

Data availability

Included in manuscript acknowledgements.

Acknowledgements

This research was funded by the Royal Society of Edinburgh (RSE) through a small research grant. Results were obtained using the ARCHIE-WeSt High-Performance Computer (www.archie-west.ac.uk) based at the University of Strathclyde. All data used in this paper are openly available through the University of Strathclyde portal,

KnowledgeBase https://doi.org/10.15129/8ded8290-1fde-41de-95f1-050eb5beb8b1.

References

Akylas, T.R., 1984. On the excitation of long nonlinear water waves by a moving pressure distribution. J. Fluid Mech. 141, 455–466. https://doi.org/10.1017/S0022112087000855.

Alam, M.R., Mei, C.C., 2008. Ships advancing near the critical speed in a shallow channel with a randomly uneven bed. J. Fluid Mech. 616, 397–417. https://doi.org/10.1017/S0022112008004035.

Bellafiore, D., Zaggia, L., Broglia, R., Ferrarin, C., Barbariol, F., Zaghi, S., Lorenzetti, G., Manfè, G., De Pascalis, F., Benetazzo, A., 2018. Modeling ship-induced waves in shallow water systems: the Venice experiment. Ocean Eng. 155, 227–239. https://doi.org/10.1016/j.oceaneng.2018.02.039.

Burmester, S., Vaz, G., el Moctar, O., 2020. Towards credible CFD simulations for floating offshore wind turbines. Ocean Eng. 209, 107237 https://doi.org/10.1016/j.oceaneng.2020.107237.

Campbell, R., Terziev, M., Tezdogan, T., Incecik, A., 2022. Computational fluid dynamics predictions of draught and trim variations on ship resistance in confined waters. Appl. Ocean Res. 126, 103301 https://doi.org/10.1016/j.apor.2022.103301.

Celik, I.B., Ghia, U., Roache, P.J., Freitas, C., 2008. Procedure for estimation and reporting of uncertainty due to discretization in CFD applications. J. Fluids Eng. 130, 078001 https://doi.org/10.1115/1.2960953.

Chen, X.-N., Sharma, S.D., 1995. A slender ship moving at a near-critical speed in a shallow channel. J. Fluid Mech. 291, 263. https://doi.org/10.1017/S0022112095002692.

Choi, H.Ter, Bai, K.J., Kim, W.J., Cho, I.H., 1991. Nonlinear free surface waves due to a ship moving near the critical speed in a shallow water. In: Proc 18th Symposium on Naval Hydrodynamics, pp. 173–189.

Cole, S.L., 1985. Transient waves produced by flow past a bump. Wave Motion 7, 579–587.

Ertekin, R.C., Webster, W.C., Wehausen, J.V., 1984a. Ship-generated solitons. In: Proc 15th Symp on Naval Hydrodynamics. Hamburg, Germany.

Ertekin, R.C., Webster, W.C., Wehausen, J.V., 1986. Waves caused by a moving disturbance in a shallow channel of finite width. J. Fluid Mech. 169, 275–292. https://doi.org/10.1017/S0022112086000630.

Ertekin, R.C., Webster, W.C., Wehausen, J.V., 1984b. Ship-generated solitons. In: 15th Symposium of Naval Hydrodynamics. Hamburg, Germany.

Fourdrinoy, J., Dambrine, J., Petcu, M., Pierre, M., Rousseaux, G., 2020. The dual nature of the dead-water phenomenology: Nansen versus Ekman wave-making drags. Proc. Natl. Acad. Sci. 117, 201922584 https://doi.org/10.1073/pnas.1922584117.

Grue, J., 2017. Ship generated mini-tsunamis. J. Fluid Mech. 816, 142–166. https://doi.org/10.1017/jfm.2017.67.

Havelock, T., 1908. The propagation of groups of waves in dispersive media, with application to waves on water produced by a travelling disturbance. Proc. R. Soc. London. Ser. A, Contain. Pap. a Math. Phys. Character, 81, 389–430. https://doi.org/10.1098/rspa.1933.0074.

Hirt, C.W., Nichols, B.D., 1981. Volume of fluid (VOF) method for the dynamics of free boundaries. J. Comput. Phys. 39, 201–225. https://doi.org/10.1016/0021-9991(81)90145-5.

Huang, D.B., Sibul, O.J., Webster, W.C., Wehausen, J.V., Wu, D.M., Wu, T.Y., 1982. Ships moving in the transcritical range. In: Proc. Conf. on Behaviour of Ships in Restricted Waters, pp. 26(1)–26(10).

Jiang, T., 1999. Investigation of waves generated by ships in shallow water. In: Twenty-Second Symposium on Naval Hydrodynamics Office of Naval Research, pp. 601–612. Washington DC.

Katsis, C., Akylas, T.R., 1987. On the excitation of long nonlinear water waves by a moving pressure distribution. Part 2. Three dimensional effects. J. Fluid Mech. 177, 49–65. https://doi.org/10.1017/S0022112087000855.

Lataire, E., Vantorre, M., Delefortrie, G., 2012. A prediction method for squat in restricted and unrestricted rectangular fairways. Ocean Eng. 55, 71–80. https://doi.org/10.1016/j.oceaneng.2012.07.009.

Lee, S.-J., Grimshaw, R.H.J., 1990. Upstream - advancing waves generated by three - dimensional moving disturbances. Phys. Fluids A Fluid Dyn. 2, 194–201.

Li, M., Yuan, Z.M., Tao, L., 2023. Wash waves generated by ship moving across a depth change. Ocean Eng. 275, 114073 https://doi.org/10.1016/j.oceaneng.2023.114073.

Li, Y., Sclavounos, P.D., 2002. Three-dimensional nonlinear solitary waves in shallow water generated by an advancing disturbance. J. Fluid Mech. 470, 383–410. https://doi.org/10.1017/S0022112002001568.

Mei, C.C., 1986. Radiation of solitons by slender bodies advancing in a shallow channel. J. Fluid Mech. 162, 53–67. https://doi.org/10.1017/S0022112086001921.

Mei, C.C., Choi, H.S., 1987. Forces on a slender ship advancing near the critical speed in a wide canal. J. Fluid Mech. 179, 59–76. https://doi.org/10.1017/S0022112087001435.

Miles, J.W., 1986. Stationary, transcritical channel flow. J. Fluid Mech. 162, 489–499. https://doi.org/10.1017/S0022112086002136.

Miles, J.W., 1980. Solitary waves. Annu. Rev. Fluid Mech. 12, 11–43. https://doi.org/10.1515/9789048505395-009.

Moreira, R.M., Chacatlana, J.T.A., Santos, J.A., Rodrigues, S.R.A., Neves, C.F., 2014. On pressure disturbance waves in channels: solitons, jets and ripples. Maritime Technol. Eng. 969–978. https://doi.org/10.1201/b17494-103.

Muscalus, A.C., Haas, K.A., 2022. Vessel wake contributions to erosion at exposed and sheltered shorelines near a tidal shipping channel. Coast. Eng. 178, 104220 https://doi.org/10.1016/j.coastaleng.2022.104220.

Pedersen, G., 1988. Three-dimensional wave patterns generated by moving disturbances at transcritical speeds. J. Fluid Mech. 196, 39–63. https://doi.org/10.1017/S0022112088002605.

Richardson, L.F., 1927. Deferred approach to the limit. Trans. R. Soc. London, Ser. A 226, 299–361.

Russell, J.S., 1845. Report on waves: made to the meetings of the British Association in 1842–43. https://doi.org/10.1038/002124a0.

Salas, M.D., 2006. Some observations on grid convergence. Comput. Fluids 35, 688–692. https://doi.org/10.1016/j.compfluid.2006.01.003.

Terziev, M., Liu, Y., Yuan, Z., Incecik, A., 2023a. The resistance of a trans-critically accelerating ship in shallow water. Ship Technol. Res. 13–32. https://doi.org/10.1080/09377255.2023.2252232.

Terziev, M., Mosse, J., Norman, R., Pazouki, K., Lord, R., Tezdogan, T., Thompson, C., Konovessis, D., Incecik, A., 2023b. Review of UK inland waterways transportation from the hydrodynamics point of view. Urban Plan. 8, 1–13. https://doi.org/10.17645/up.v8i3.6752.

Terziev, M., Tezdogan, T., Incecik, A., 2022. Scale effects and full-scale ship hydrodynamics: a review. Ocean Eng. 245, 110496 https://doi.org/10.1016/j.oceaneng.2021.110496.

Terziev, M., Tezdogan, T., Incecik, A., 2021. A numerical assessment of the scale effects of a ship advancing through restricted waters. Ocean Eng. 229, 108972 https://doi.org/10.1016/j.oceaneng.2021.108972.

Terziev, M., Tezdogan, T., Incecik, A., 2020. Modelling the hydrodynamic effect of abrupt water depth changes on a ship travelling in restricted waters using CFD. Ships Offshore Struct. https://doi.org/10.1080/17445302.2020.1816731.

Terziev, M., Tezdogan, T., Incecik, A., 2019. Application of eddy-viscosity turbulence models to problems in ship hydrodynamics. Ships Offshore Struct. 1–24. https://doi.org/10.1080/17445302.2019.1661625.

Thews, J.G., Landweber, L., 1935. The influence of shallow water on the resistance of a cruiser model. In: US Exp. Model Basin Rep. 408. Washington, DC, Navy Yard 46.

Torsvik, T., Didenkulova, I., Soomere, T., Parnell, K.E., 2009. Variability in spatial patterns of long nonlinear waves from fast ferries in Tallinn Bay. Nonlinear Process. Geophys. 16, 351–363. https://doi.org/10.5194/npg-16-351-2009.

Wilcox, D.C., 2008. Formulation of the k-w turbulence model revisited. AIAA J. 46, 2823–2838. https://doi.org/10.2514/1.36541.

Wu, D.-M., Wu, T.Y., 1982. Three-dimensional nonlinear long waves due to moving surface pressure. In: 14th Symposium on Naval Hydrodynamics. Ann Arbor.

Zabusky, N.J., Kruskal, M.D., 1965. Interaction of "solitons" in a collisionless plasma and the recurrence of initial states. Phys. Rev. Lett. 15, 240–243. https://doi.org/10.1017/S0022377800009648.